Analysis of Phase Separation in High Performance PbTe–PbS Thermoelectric Materials

*Steven N. Girard, Klaus Schmidt-Rohr, Thomas C. Chasapis, Euripides Hatzikraniotis, B. Njegic, E. M. Levin, A. Rawal, Konstantinos M. Paraskevopoulos, and Mercouri G. Kanatzidis**

Phase immiscibility in PbTe–based thermoelectric materials is an effective means of top-down synthesis of nanostructured composites exhibiting low lattice thermal conductivities. $PbTe_{1-x}S_x$ thermoelectric materials can be synthesized as metastable solid solution alloys through rapid quenching. Subsequent post-annealing induces phase separation at the nanometer scale, producing nanostructures that increase phonon scattering and reduce lattice thermal conductivity. However, there has yet to be any study investigating in detail the local chemical structure of both the solid solution and nanostructured variants of this material system. Herein, quenched and annealed (i.e., solid solution and phase-separated) samples of PbTe–PbS are analyzed by in situ high-resolution synchrotron powder X-ray diffraction, solid-state ^{125}Te nuclear magnetic resonance (NMR), and infrared (IR) spectroscopy analysis. For high concentrations of PbS in PbTe, e.g., x >16%, NMR and IR analyses reveal that rapidly quenched samples exhibit incipient phase separation that is not detected by state-of-the-art synchrotron X-ray diffraction, providing an example of a PbTe thermoelectric "alloy" that is in fact phase inhomogeneous. Thermally-induced PbS phase separation in PbTe–PbS occurs close to 200 °C for all compositions studied, and the solubility of the PbS phase in PbTe at elevated temperatures >500 °C is reported. The findings of this study suggest that there may be a large number of thermoelectric alloy systems that are phase inhomogeneous or nanostructured despite adherence to Vegard's Law of alloys, highlighting the importance of careful chemical characterization to differentiate between thermoelectric alloys and composites.

1. Introduction

Thermoelectric materials hold promise as environmentally friendly heat-to-electric power generators, but are limited by low efficiencies. The efficiencies of thermoelectric materials are related to the thermoelectric figure of merit (ZT). For conventional bulk thermoelectric materials, such as Bi_2Te_3, PbTe, and SiGe, values of ZT have been limited to approximately 1.[1–5] Recently, research toward increasing the ZT of thermoelectric materials has succeeded using the concept of nanostructuring. By incorporating nanostructures, the lattice thermal conductivity (κ_{lat}) may be significantly reduced through phonon scattering, preferably without a significant reduction in carrier mobility, resulting in enhanced ZT.[1,4] Reductions in lattice thermal conductivity have been observed in high-ZT thin-film materials,[6,7] nanomaterials,[8,9] and nanostructured bulk materials.[10] In particular, nanostructured bulk materials hold promise because their apparent ease in scalability and synthesis makes them immediately attractive for commercial fabrication of thermoelectric devices in the very near future.

Dr. S. N. Girard, Dr. T. C. Chasapis
Department of Chemistry
Northwestern University
Evanston IL 60208, USA
Prof. K. Schmidt-Rohr
Department of Chemistry
Iowa State University
Ames, IA 50011, USA
Prof. K. Schmidt-Rohr, Dr. B. Njegic, Dr. E. M. Levin, Dr. A. Rawal
Division of Materials Sciences and Engineering
Ames Laboratory U.S. DOE, Ames, IA 50011, USA
Dr. T. C. Chasapis, Dr. E. Hatzikraniotis,
Prof. K. M. Paraskevopoulos
Physics Department
Aristotle University of Thessaloniki
GR- 54124, Thessaloniki, Greece
Prof. M. G. Kanatzidis
Department of Chemistry
Northwestern University
Evanston IL 60208, USA
E-mail: m-kanatzidis@northwestern.edu
Prof. M. G. Kanatzidis
Materials Science Division
Argonne National Laboratory U.S. DOE
Argonne, IL 60439, USA

DOI: 10.1002/adfm.201201944

Recent attempts to control the formation of nanostructures in bulk thermoelectric materials involve a microstructure engineering approach whereby phase-separation processes are manipulated to generate a nanoscale second phase that is embedded within the parent thermoelectric material. This has been demonstrated in PbTe and GeTe systems using a variety of approaches, including precipitation,[11–13] nucleation and growth and spinodal decomposition,[14–16] eutectic,[17–20] and matrix encapsulation methods.[21,22] In each of these examples, the parent "matrix" material and second minor phase must be judiciously chosen considering phase stability and compatibility in thermoelectric properties. Many of these systems utilize natural phase separation and precise thermal treatment to selectively cause the minor phase to precipitate as nanostructures <100 nm. Some systems, such as those exhibiting reversible phase-separation phenomena,[14–16] are especially interesting because the nucleation and coarsening of minor phases may be systematically controlled by thermal treatment.

We recently showed that the $PbTe_{1-x}$ S_x (alternatively, PbTe–PbS x%) thermoelectric materials system may be thermally manipulated to selectively create solid-solution and nanostructured analogues.[23] From these studies, it was found that the reduction in lattice thermal conductivity was more pronounced in the nanostructured samples compared with the solid solutions, resulting in enhanced ZT. This system is one of the highest performing thermoelectric materials to date, with values of ZT from 1.5 to 1.8 at 700–800 K.[24] These large values of ZT are caused either directly or in part by low lattice thermal conductivity, produced by phonon scattering at the interfaces of coherent PbS nanostructures embedded within the PbTe matrix. We have previously shown that solid solutions of PbTe–PbS 8% measured from room temperature to 700 K exhibit nanoscale phase separation and a significant reduction in lattice thermal conductivity.[23] The PbTe–PbS system exhibits a miscibility gap where thermodynamic phase separation will occur by metastable nucleation and growth or unstable spinodal decomposition processes; see **Figure 1** a.[25–29] Nucleation and growth and spinodal decomposition phase transformations occur because of the distinct curvature in the Gibbs free energy (G) curve for a given isotherm over the composition range x as the material transforms to reduce the overall free energy of the system.[30]

In the nucleation and growth region, normally at the outer extremes of the composition range, the free energy curve has positive curvature (i.e., opens "upward" like the letter u) expressed as $\partial^2G/\partial x^2 > 0$. This means small variations in composition in this range lead to an increase in free energy. Rapidly cooled solid solutions are thermodynamically metastable, and the free energy can only be decreased if nuclei with a drastically different composition are generated, typically by thermal treatment. Once nuclei are formed, "down-hill" diffusion causes particle coarsening through the desaturation of atoms of the minor phase in the surrounding matrix. Conversely, spinodal decomposition occurs toward the inner part of the composition range, where the free energy curve has negative curvature (i.e., opens "downward" like the letter n) expressed as $\partial^2G/\partial x^2 < 0$. Because small changes in composition reduce the free energy, the material will immediately form minute compositional fluctuations that will coarsen through an 'uphill' diffusion process. This means that rapidly cooled solid solutions are thermodynamically unstable and should spontaneously decompose into a two-phase mixture regardless of thermal treatment.

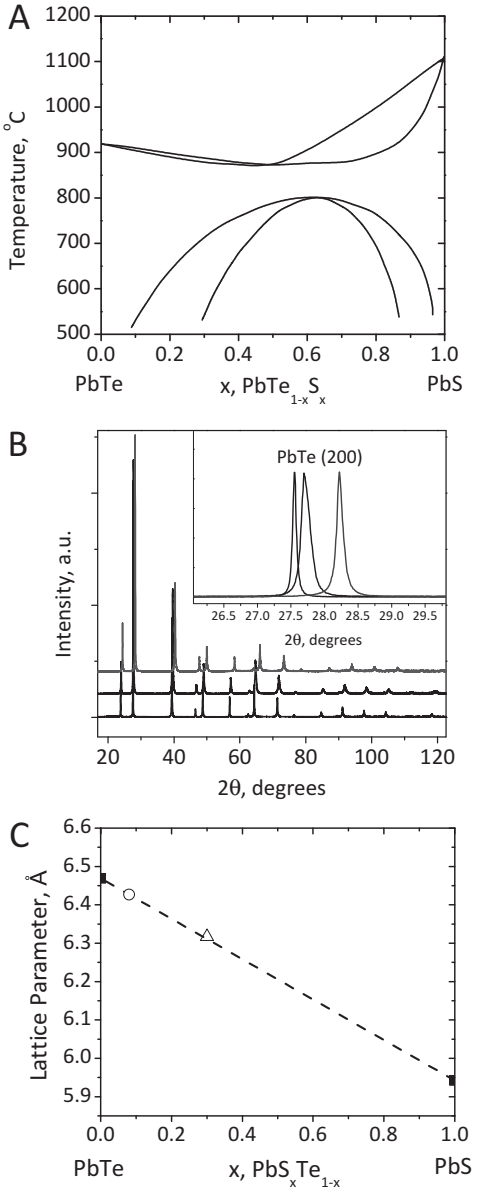

Figure 1. a) Experimentally derived PbTe–PbS phase diagram, adapted with permission.[29] b) High-resolution PXRD of quenched PbTe (bottom), PbTe–PbS 8% (middle), and PbTe–PbS 30% (top). The inset shows the contraction of the PbTe lattice for the (200) Bragg reflection moving from quenched PbTe (leftmost peak), PbTe–PbS 8% (middle peak), and PbTe–PbS 30% (rightmost peak). Rapidly quenched samples of PbTe–PbS create a single-phase cubic phase (space group Fm3m) with a homogeneous distribution of S and Te at the cationic sites of the crystal lattice. c) Lattice parameters of samples from b) showing nearly ideal solid-solution alloying of quenched PbTe–PbS 8% (open circle) and PbTe–PbS 30% (open triangle).

To date, there has yet to be a systematic study addressing the thermodynamic and kinetic phase interactions within the pseudo-binary PbTe–PbS system. Ideally, a firm understanding

of the temperatures of nanoparticle nucleation may enable the engineering of the size and relative dispersion of PbS nanoparticles within PbTe, and correspondingly tune the thermoelectric properties. Recently, Ikeda et al.[31,32] and Gorsse et al.[15] have reported systematic annealing studies for PbTe-based materials, wherein the coarsening of microstructures may be controlled by thermal treatment. However, for such phase immiscible systems the nanostructured phase will also dissolve in the matrix at sufficiently high temperatures. The exact temperatures where this occurs should be determined in order to take full advantage of nanostructures to reduce lattice thermal conductivity.

In this paper, we investigate the chemical phase stability in the PbTe–PbS thermoelectric system using a variety of spectroscopic and physiochemical analyses to understand the formation of nanostructures. It has already been demonstrated that phase-separated nanodomains in PbTe–PbS produce low values of lattice thermal conductivity.[16,23,24] Herein, we analyze quenched and annealed (i.e., solid solution and phase-separated) samples of PbTe–PbS by in situ high-resolution synchrotron powder X-ray diffraction (PXRD), solid-state ^{125}Te nuclear magnetic resonance (NMR), and infrared (IR) spectroscopy analysis. For high concentrations of PbS in PbTe (>16%), we show that rapidly quenched samples exhibit incipient phase separation, despite adherence to Vegard's law of alloys as determined by X-ray diffraction, providing another example of a seemingly PbTe thermoelectric "alloy" that is in fact phase inhomogeneous.[33] We show that thermally-induced PbS phase separation in PbTe–PbS occurs close to 200 °C and report the solubility of PbS in PbTe at elevated temperatures >500 °C. Many reports within the field of thermoelectrics and beyond have evidenced solid solutions by adherence to Vegard's law and simple X-ray characterization; this work emphasizes the importance of careful chemical and microstructural characterization that is paramount in adequately describing the differences between thermoelectric materials asserted to be either alloyed or nanostructured.

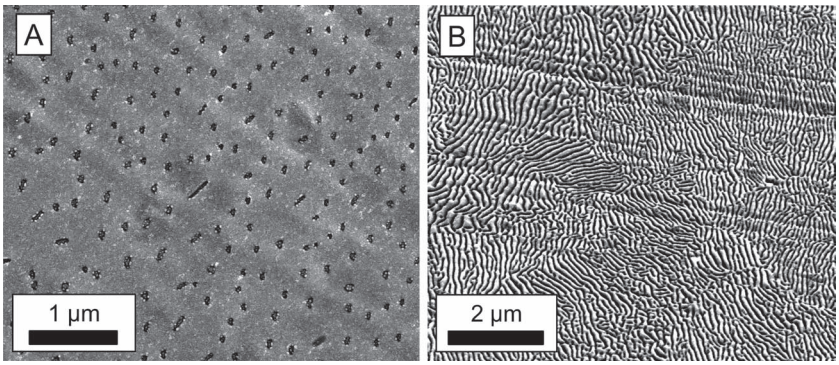

Figure 2. Microstructure of phase-separated (annealed) PbTe–PbS of different compositions: a) 8% and b) 30%. The 30% composition phase separates by spinodal decomposition, producing an interconnected labrythine network of PbS (dark regions) throughout the PbTe matrix, while nucleation and growth in the 8% composition produces spherical nuclei of PbS (dark regions) within the PbTe matrix.

2. Results and Discussion

2.1. High-Resolution PXRD of PbTe–PbS

We initially needed to verify that PbTe–PbS materials could successfully generate genuine solid-solution alloys upon rapid quenching directly from the melt. We specifically chose the PbTe–PbS 8 and 30% compositions for several reasons: 1) both exhibit low lattice thermal conductivity, presumably from nanostructuring;[16] 2) they phase separate by differing processes (nucleation and growth and spinodal decomposition, respectively); 3) both compositions have been extensively studied in our research group;[23,34] and 4) given limited beam time at the Advanced Photon Source (APS), we preferentially chose to closely study these compositions. High-resolution powder X-ray diffraction of rapidly cooled PbTe–PbS 8 and 30% are shown in Figure 1b. The lattice parameter (d-spacing) of the PbTe matrix monotonically decreases with increasing PbS incorporation, and the samples obey Vegard's law (Figure 1c).

The microstructure examined by scanning electron microscopy (SEM) of as-quenched samples of undoped PbTe–8% PbS and 30% PbS does not exhibit any large PbS precipitates. Once annealed at 500 °C for 72 h, the samples undergo clear PbS phase separation. The PbTe–PbS 8% sample shows mostly spherical precipitates with an average diameter of 100 nm (**Figure 2** a). As a result of the nucleation and growth phase transformation, mostly spherical particles are observed. Conversely, the PbTe–PbS 30% sample exhibits a labyrinthine network structure of interconnected PbS-rich regions (Figure 2b). The slight compositional fluctuations that coarsen with time as a result of spinodal decomposition result in interconnected rod-like lamellar structures. The average width of the PbS precipitates is ≈100 nm and they can extend microns in length. Energy dispersive X-ray spectroscopy (EDS) verified the presence of the PbS phase in the annealed samples. However, elemental analysis by EDS was unsuccessful for the solid solution samples because of the close overlap in the M and K lines of Pb and S, respectively. We did not include any transmission electron microscopy (TEM) in this study, as it has been reported in detail previously.[23,34]

In order to better understand the onset of nanostructure generation, the solid-solution PbTe–PbS 8 and 30% samples were initially analyzed by synchrotron high-resolution PXRD using a high-temperature blower heating at 5 °C/min. The results are shown in **Figure 3**. For the PbTe–PbS 8% sample, PbS reflections become visible above 250 °C (Figure 3a). The region of immiscibility is roughly in the range of 200 to 500 °C. The temperature of dissolution of PbS at approximately 500 °C is in close agreement with the phase diagram published by Leute, reproduced in Figure 1a.[29] For the PbTe–PbS 30% sample, a significant precipitation of PbS is observed between 250 and 700 °C (Figure 3c). Additionally, above ≈550 °C the movement of the sample from the spinodal to the nucleation and growth region (see Figure 1a) results in increased dissolution of S into

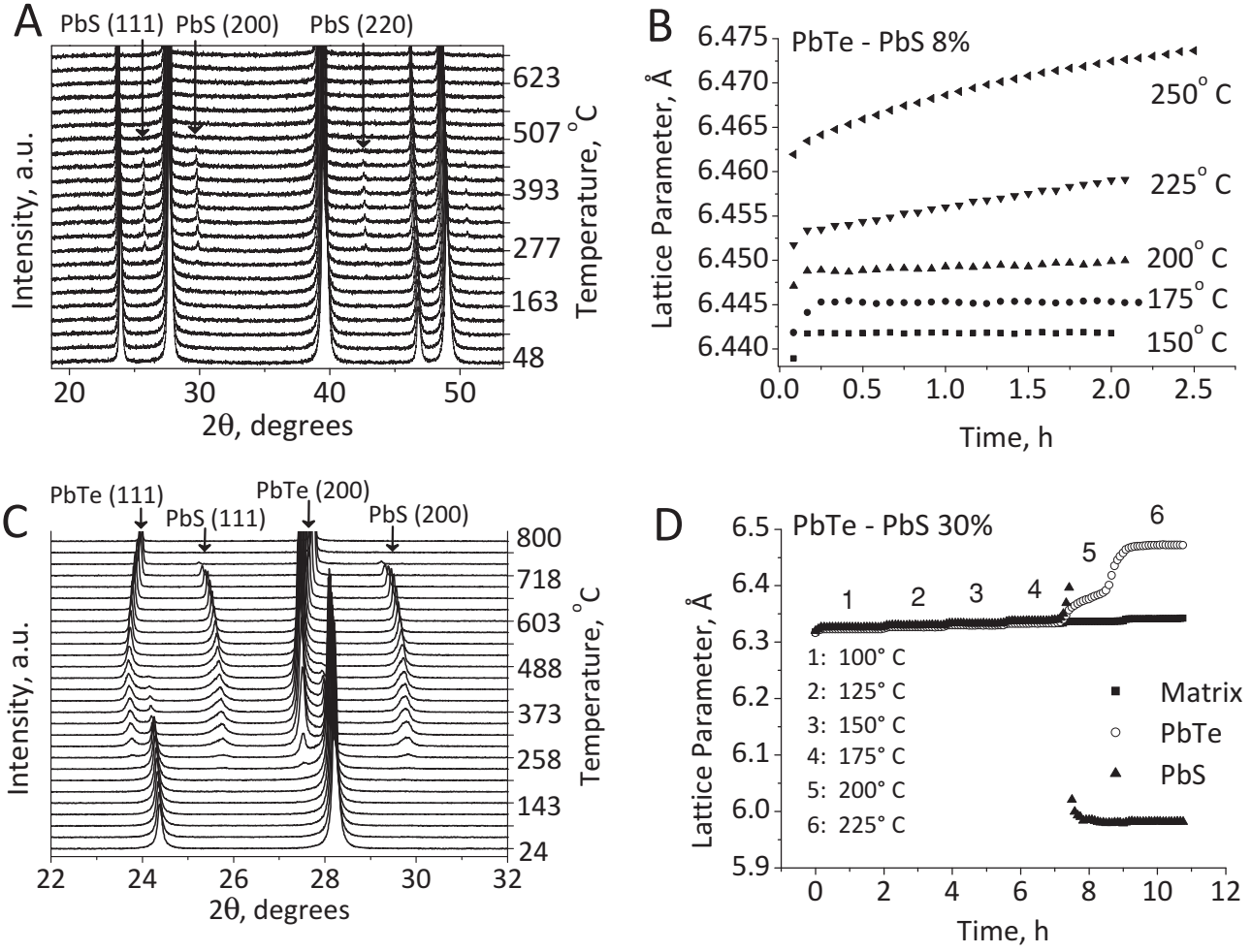

Figure 3. High temperature phase stability of PbTe–PbS. a) In situ high-temperature PXRD of PbTe–PbS 8% solid-solution alloys. The precipitation of PbS is evidenced by the appearance of PbS (111), (200), and (220) reflections between 200 and 500 °C. At temperatures >500 °C, the PbS redissolves into the PbTe matrix, re-forming a solid solution. b) In situ high-temperature PXRD of PbTe–PbS 30% solid-solution alloys. The precipitation of PbS is evidenced as in Figure 4. The higher PbS concentration produces a region of immiscibility between 250 and 750 °C. At temperatures >750 °C, the PbS redissolves into the PbTe matrix, re-forming a solid solution. c) Rietveld refinements of lattice parameters for annealing studies of PbTe matrix in PbTe–PbS 8%, and d) PbS_{1-x} Te_x solid solution, PbTe, and PbS phases in PbTe–PbS 30%. Each sample was heated for two hours at the temperatures indicated. For both samples, significant PbS precipitation is initiated at temperatures at and above 200 °C; in (c) this is evidenced by a slight increase in the third annealing step, and in (d) this is evidenced by the sudden appearance of PbS and PbTe reflections. The slight increase in PbS lattice parameter at the onset of precipitation is an artifact of poor refinement caused by the minute PbS peak generated at the onset of precipitation.

PbTe and Te into PbS, contracting the PbTe and expanding the PbS lattices, in agreement with the lever rule. We show that PbTe–PbS behaves ideally, and that we may selectively generate solid-solution alloys and phase-separated samples depending on thermal treatment.

In order to more precisely determine the temperature of phase separation for PbTe–PbS 8 and 30%, we performed selective annealing studies of the samples around the lower temperature of immiscibility. For PbTe–PbS 8%, we heated in five 25° steps from 150–250 °C, while for PbTe–PbS 30%, we heated in six 25 °C steps from 100–225 °C (Figure 3b,d). At each temperature step, the sample was held for two hours while repeated diffraction scans were collected. We then analyzed the diffraction patterns by Rietveld refinements, to accurately determine the effect of the annealing temperatures without thermal expansion of the lattice or thermal smear. For PbTe–PbS 8%, we indexed only major peaks of PbTe because the PbS peaks were too small to accurately refine. The PbTe matrix shows monotonic thermal expansion of the lattice for the first two annealing steps without any change in lattice parameter over time (Figure 3b). At the 200 °C annealing step, a slight but perceptible increase of the lattice parameter is observed over time. This shows that precipitation of PbS in PbTe–PbS 8% solid-solution alloys is initiated between 175 and 200 °C, in close agreement with our previous in situ properties measurements.[23] At higher temperatures, the lattice parameter increases more rapidly as a consequence of enhanced PbS dissolution within the PbTe matrix at elevated temperatures. For PbTe–PbS 30%, the precipitation of distinct

PbS and PbTe phases is detected almost immediately after 200 °C has been reached (Figure 3d). For both samples, the kinetic barriers to significant phase separation appear to be overcome at temperatures close to 200 °C. In future studies, this information may be utilized to create systematically size-controlled nanostructures by limiting the coarsening of the particles following nucleation.

2.2. ^{125}Te NMR of Solid-Solution PbTe–PbS

In order to gain a deeper understanding of the chemical structure of quenched and of annealed PbTe–PbS materials, we conducted ^{125}Te NMR to determine the local structure of the PbTe-rich matrix.[35–39] We synthesized PbTe–PbS 4, 8, 16, 30, and 50% samples that had been quenched to generate solid-solution alloys, and then annealed to phase separate. **Figure 4** shows the ^{125}Te NMR spectra of the solid-solution materials. At low sulfur concentrations, the major peak is observed near –1850 ppm, close to the resonance position of PbTe,[35] as expected. Additionally, there are smaller peaks just to the right of the main signal that successively grow in intensity with increasing PbS concentration, x. These must be attributed to sulfur atoms producing a chemical shift at a nearby ^{125}Te nucleus, with an increment of approximately –140 ppm per sulfur. They cannot be due to different Knight shifts (resulting from different charge carrier concentrations), since the T_1 relaxation times of all the signals are similar; a change in Knight shift by –140 ppm in PbTe corresponds to a change in T_1 relaxation time by orders of magnitude.[35–37] Furthermore, a peak position of –2000 ppm in PbTe due to Knight shift would indicate p-type doping,[36] while the present samples are n-type semiconductors.

In the NaCl structure of PbTe–PbS, each tellurium has 18 second neighbor sites on the Te sublattice that can be occupied by S, see the inset in Figure 4. The probability of exactly n sulfur neighbors out of N total is given by a binomial formula,[39]

$$P_{x,N}(n) = x^n (1-x)^{N-n} \binom{N}{n} \quad (1)$$

However, the bar graphs produced based on this formula with $N = 18$, see Figure 4a, do not provide good fits to the measured spectra. For instance, at small x, the fraction of Te with a S neighbor is $P_{x,18}(1) = 18x(1–x)^{17}$. For $x = 0.04$, this predicts $P_{x,18}(1) = 0.36$, while the area fraction under the corresponding peak is only 0.2.

On the other hand, the NMR spectra are easy to explain if there are only up to $N = 6$ (rather than 18) sulfur neighbors of a given tellurium that produce significant chemical shifts. An analysis in that light (see inset in Figure 4) shows that there are 6 second neighbors along two collinear bonds (filled black circles), and 12 with the two bonds at a right angle (filled gray circles), in the NaCl crystal structure. We interpret our data as showing that sulfur has strong effects on the ^{125}Te chemical shift only in the former $N = 6$ sites. Figure 4b shows bar graphs

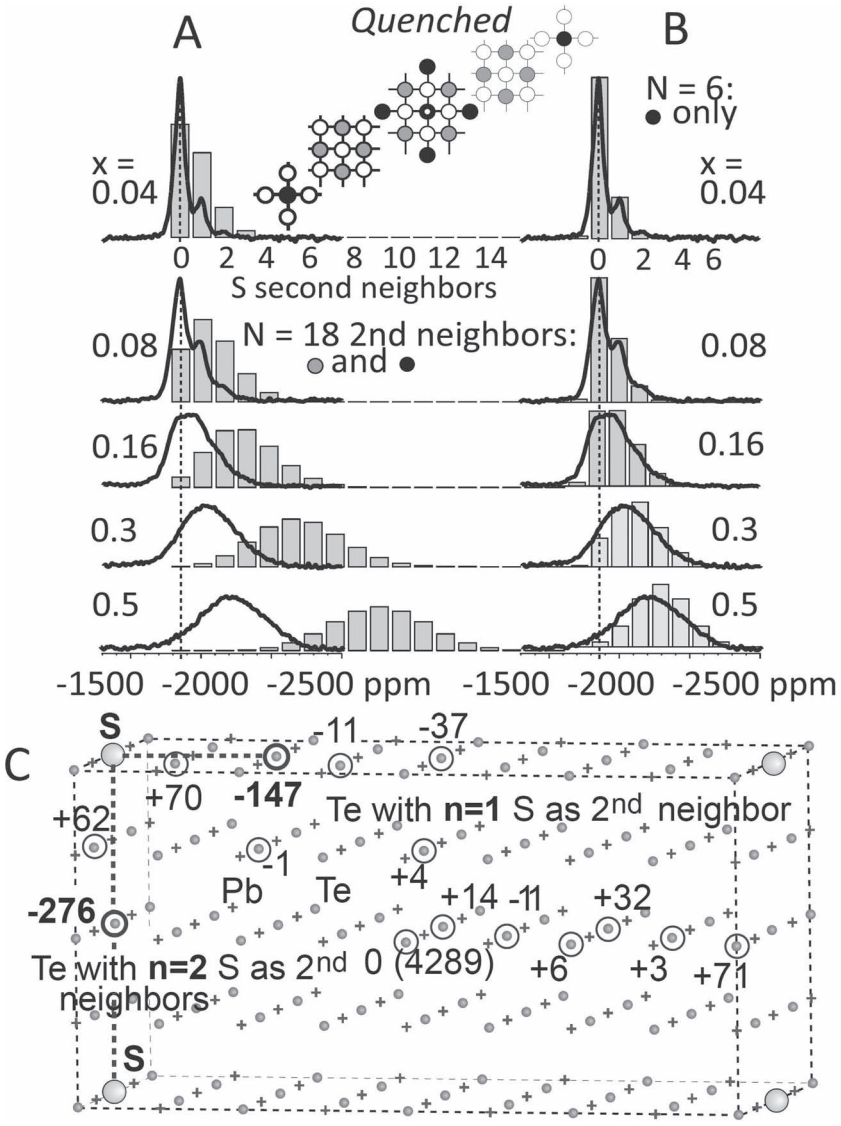

Figure 4. a,b) ^{125}Te NMR spectra of quenched $PbTe_{1-x}S_x$ for $x = 0.04$, 0.08, 0.16, 0.3, and 0.5. While the total area decreases with decreasing tellurium fraction, proportional to (1–x), in the figure the spectra have been scaled to equal area for clarity. a) Spectra with overlaid bar graphs for up to N = 18 sulfur neighbors producing chemical shifts of –140 ppm. b) Same as (a) but with bar graphs for N = 6. Better fits for $x = 0.3$ and 0.5 based on a spinodal-decomposition model are shown in Figure 5. First-order spinning sidebands included in these simulations produce two small extra bars on the left and right ends of the distribution. The inset (top center) shows five planes in the NaCl structure of PbTe with the 18 neighbors on the Te sublattice highlighted. The N = 6 sites apparently producing significant ^{125}Te chemical shift effects are marked by filled black circles. c) Calculated ^{125}Te isotropic chemical shifts in ppm with respect to the least perturbed tellurium atom (shielding given in brackets) in PbTe doped with a single sulfur atom, in a $PbTe_{0.98}S_{0.02}$ unit cell optimized in P4/mmm symmetry with calculated lattice parameters of 13.11 Å × 13.11 Å × 26.22 Å. The tellurium atoms are shown as small balls, lead atoms as crosses, and sulfur atoms as large balls.

using $N = 6$ in Equation (1), which provide good fits of the measured spectra up to $x = 0.16$.

In order to provide a convincing confirmation of the hypothesis regarding the differential effect of different Te-Pb-S geometries, ^{125}Te NMR chemical shifts were calculated using density functional theory (DFT) for 64-atom and 128-atom unit cells of PbTe in which a single tellurium atom was substituted by sulfur (for technical details see the Supporting Information). Such ab initio DFT calculations can provide unique insights into the effects of dopants on ^{125}Te chemical shifts. A single S atom collinearly bonded to tellurium (^{125}Te-Pb-S) shows a shift of –147 ppm, and two sulfur impurities in a collinear S-Pb-^{125}Te-Pb-S arrangement cause a shift of –276 ppm (see Figure 4 and Figure S1 in the Supporting Information). These predicted ^{125}Te chemical shifts are in excellent agreement with the experimental data. When the S-Pb bond is perpendicular to the Pb-Te bond, the calculated shift is of smaller magnitude and opposite sign, even though this arrangement places S closest to the tellurium atom. Therefore, both calculated and experimental data identify a collinear ^{125}Te-Pb-S motif as producing the observed large negative change of about –140 ppm in the ^{125}Te chemical shift.

For solid-solution samples of PbTe–PbS 30 and 50%, the maxima in the bar graphs simulated based on Equation (1) are to the right of the maxima in the experimentally observed spectra, see Figure 4b. This could mean that the PbTe-rich phase observed here contains less sulfur than the nominal composition; simulations with $x_{\text{Te-rich}} = 0.26$ and 0.45 for nominal $x = 0.3$ and 0.5, respectively, are shown in **Figure 5**a,b.

Good fits were also obtained for a model that approximates the results of the spinodal decomposition expected in this concentration region. This is consistent with the onset of spinodal decomposition deduced in the quenched $x = 0.5$ sample from detailed analysis of scattering data.[40] Spinodal decomposition produces a periodic modulation of the composition in space. This results in a distribution of local compositions, but the main contributions are from the minimum and maximum values of x. Therefore, we simulated the spectrum as resulting from two local environments of equal volume and compositions $x + \Delta x$ and $x - \Delta x$.

$$P_{Sp}(n) = 1/2\ \left[P_{x+\Delta x,6}(n)\ (1-(x+\Delta x))/(1-x) + P_{x-\Delta x,6}(n)(1-(x-\Delta x))/(1-x)\right] \quad (2)$$

where each component is weighted with its ^{125}Te NMR signal fraction, which is the fraction of Te, $(1-(x\pm\Delta x))$. Fits based on this model are shown in Figure 5c and d. The shift in the maximum of $P_{Sp}(n)$ to the left is due to the larger Te signal of the Te-rich component, which has its maximum at lower n (due to less S). The width of $P_{Sp}(n)$ is larger since two unequal distributions are added together; this improves the quality of the fit for the nominal 30 and 50% compositions.

The analysis provides clear evidence of incipient spinodal decomposition, increasing towards the center of the miscibility gap. The best fits give an indication of the amplitude $2\Delta x$ to the composition difference between the Te-rich and Te-poor regions, but with significant uncertainties, not least because of the over-simplifications inherent in the two-component model used. Indeed, these samples exist as macroscale "solid solutions" with a largely homogeneous medium as evidenced by PXRD. However, by ^{125}Te NMR (and IR reflectivity below), we show that nascent spinodal decomposition is present in these samples, likely as minute regions that are slightly off-stoichiometry relative to the nominal concentrations of PbTe and PbS.

2.3. ^{125}Te NMR of Phase-Separated PbTe–PbS

Figure 6 compares the ^{125}Te NMR spectra for solid-solution PbTe–PbS in the left column (panels a–e) with corresponding spectra for annealed samples to the right (panels f–j). For small sulfur content ($x \leq 0.08$), annealing changes the spectra only slightly. However, for $x > 0.16$, the ^{125}Te spectra of the annealed samples exhibit a pattern similar to that of the quenched material with $x = 0.08$; the best fit value is $x = 0.065$. Since most Te is found in the Te-rich phase, the dominant signals in the ^{125}Te spectra are from this component. Thus, our spectra show that after annealing the PbTe-rich phase contains 7 ± 1% S, in good agreement with the lever rule applied to the phase diagram (Figure 1a). This shows that the assumption of Lin et al.[40] that the PbTe-rich phase is pure PbTe is not justified; apparently, analysis of the pair correlation function cannot detect substitution of Te by S at the 7% level in a multiphase material.

This composition, and even more directly the relatively minor spectral change upon annealing for $x = 0.08$, means that in the annealed $x = 0.08$ sample studied here only a small fraction of sulfur ($\Delta x = -0.01 \pm 0.015$) may have precipitated to form micrometer- or nanometer-scale inclusions of PbS (1 ± 1 atom% of PbS). This is consistent with the

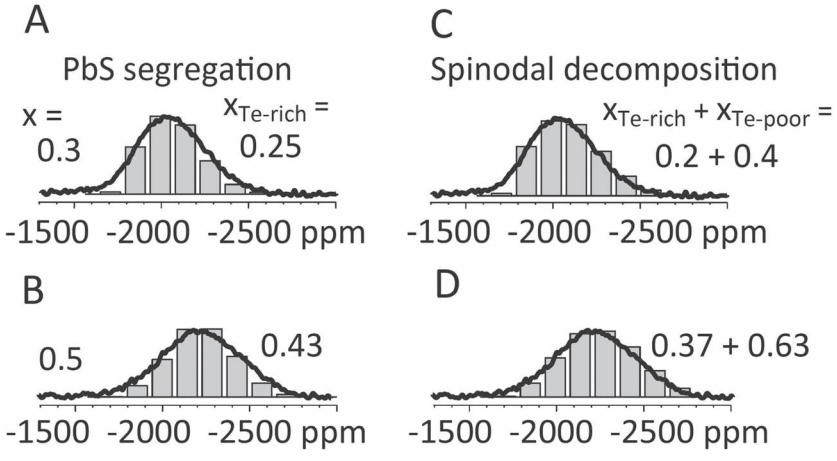

Figure 5. ^{125}Te NMR spectra of quenched $PbTe_{1-x}S_x$ for $x = 0.3$ and 0.5 compared with bar graphs from models assuming incipient phase separation. a,b): Model assuming segregation of nearly pure PbS, with negligible ^{125}Te NMR signal. c,d): Two-component model approximating spinodal decomposition. We find that the model presented in (c,d) provides a more accurate approximation of the composition, assuming that the early onset of spinodal decomposition has produced regions of inhomogeneous $PbTe_{1-x}S_x$ alloying throughout the matrix.

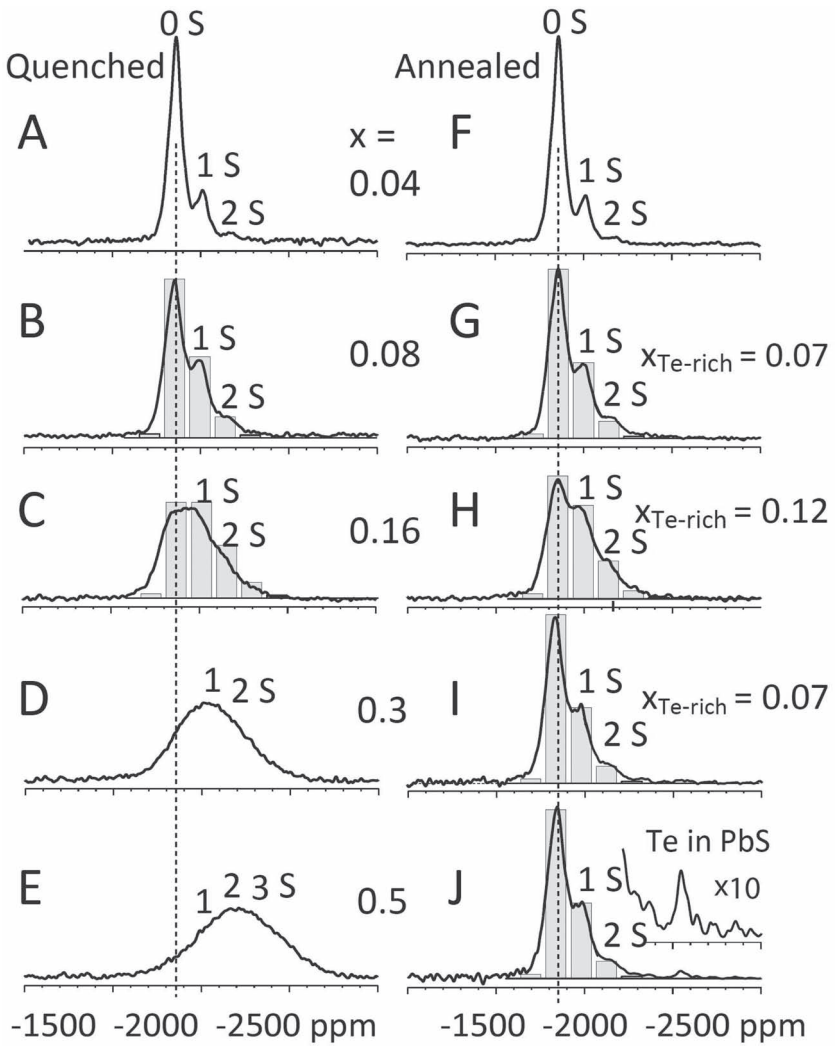

Figure 6. ^{125}Te NMR spectra of a–e) quenched and f–j) annealed PbTe–PbS with compositions: 4, 8, 16, 30, and 50% PbS. The inset in (j) shows the sharp peak of Te in PbS near –2550 ppm with 10-fold vertical expansion. While the total area decreases with decreasing tellurium fraction, proportional to (1–x), in the figure the spectra have been scaled to equal area.

X-ray data, which show no peaks of PbS but only a peak shift in 2θ by 0.08°,[23] which appears to correspond to a sulfur content reduced by Δx = –0.02 to –0.03 (i.e., 2 to 3%) in the PbTe-rich phase.

Our data are internally consistent with the following model, which in particular explains why the annealed x = 0.16 sample shows a higher S content in the PbTe-rich phase than the other annealed samples. Namely, after annealing at 500 °C for 72 h, x = 0.0(70 ± 15) is the stable composition, which is quickly reached from within the region of spontaneous decomposition inside the spinodal curve (for the x = 0.3 and x = 0.5 samples). For x = 0.16, which is in the intermediate region between nucleation-and-growth and spinodal decomposition, x = 0.12 is observed as the average composition of the PbTe-rich component of our sample. Interestingly, this is also the sample composition that has been observed to have the largest S alloying in PbTe for our p-type Na doped PbTe–PbS system.[24] We believe that the phase separation at the boundary of the two transformations may result in a sample with increased S substitution by Te. Incomplete phase separation of the annealed x = 0.16 material was also found by Lin et al.[40]

2.4. Te in the PbS-Rich Phase

Although the PbS phase is the minority phase in the samples studied here, it is interesting to examine its composition to determine Te incorporation; we refer to this as the PbS-rich phase. The amount of Te in the PbS-rich phase is small. Nevertheless, this dispersed tellurium is detectable as a small sharp peak in the ^{125}Te spectrum for x = 0.5 in Figure 6j at ≈–2550 ppm, quite close to the position expected for n = 6 (i.e., near –1840 ppm + 6 (–140 ppm) = –2680 ppm). Its area corresponds to f_d = 2% of the total intensity. On this basis (see the Supporting Information for detailed calculations), we can conclude that the PbS-rich phase contains about 2% PbTe, which is in good agreement with the phase diagram (Figure 1a) at the annealing temperature of 500 °C. In ^{207}Pb NMR (not shown), attempts to resolve signals of Pb bonded to different numbers of S atoms, or just of the PbS-rich phase, were not successful, due to line broadening that is larger than the ≈600–ppm chemical shift difference between PbTe and PbS. The line widths probably resulted from a range of Knight shifts (which reflect the local charge carrier concentration); due to a difference in the strength of the hyperfine couplings, the ^{207}Pb Knight shifts in PbTe are about 25 times larger (in ppm) than those of ^{125}Te.[41]

2.5. Infrared Reflectivity of PbTe–PbS

We conducted infrared (IR) reflectivity studies of solid-solution and phase-separated PbTe–PbS 8 and 30% samples at room temperature in order to better understand the chemical structure in light of the NMR results. Through excitations of optical and phonon modes, IR reflectivity can give us useful information regarding the sample composition: the as-obtained spectra and calculated fittings may provide information determining if the material is single or multiphase, the chemical composition of the phases, as well as phonon modes resulting from the chemical structure.

The IR reflectivity spectra of the PbTe–PbS samples displayed in **Figure 7** a show increased reflectivity values ≈90% in the low frequency range, and reflectivity minima in the frequency range ≈200–500 cm^{-1}. For all the studied compositions the reflectivity spectra show features in the frequency range ≈100–160 cm^{-1}. These features are associated with transverse

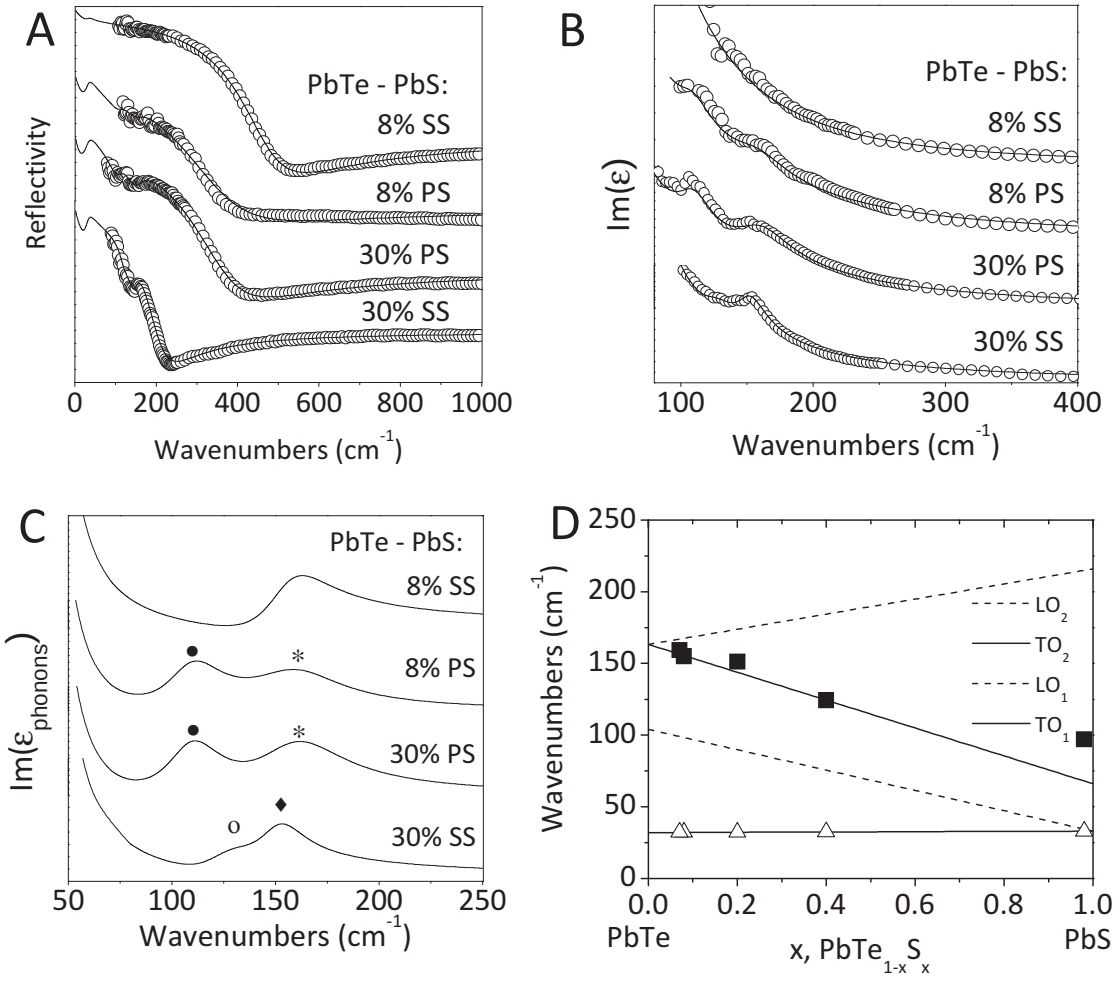

Figure 7. IR reflectivity of solid-solution and phase-separated PbTe–PbS 8% and PbTe–PbS 30% compositions. a) Experimental IR reflectivity spectra (open circles) and best fit calculated (solid lines)–spectra are shifted vertically 30% for clarity– and b) Kramers-Kronig obtained Im(ε) spectra (open circles) and the best fit calculated (solid lines) of PbTe–PbS 8% and PbTe–PbS 30% compositions. SS stands for the solid solutions and PS stands for the phase-separated samples. c) Best fit calculated TO phonons contribution to the Im(ε) spectra of the PbTe–PbS studied compositions. The increased values of the Im($\varepsilon_{phonons}$) spectra in the low frequency range are attributed to the ≈32 cm^{-1} TO phonon mode used in Equation (3) for all the studied samples (for details see text). Symbols refer to the phonon frequencies of the different phases with the latter determined by NMR; (●) $PbTe_{0.02}S_{0.98}$, (*) $PbTe_{0.93}S_{0.07}$, (○) $PbTe_{0.6}S_{0.4}$, and (♦) $PbTe_{0.8}S_{0.2}$. d) Solid lines are the interpolation lines showing the concentration dependence of the optical mode frequencies (TO-LO pairs) of $PbTe_{1-x}S_x$ mixed crystals.[42] Symbols stand for the analyzed TO frequencies of the PbTe–PbS 8% and 30% compositions, solid solutions and phase-separated, with the *x* values deduced from the NMR results.

optical (TO) phonon modes associated with Pb-Te and Pb-S vibrations, and are observed in the Kramers-Kronig obtained Im(ε) spectra of Figure 7b. The Im(ε) spectra display increased values in the low frequency range denoting free carrier effects which are associated with the reflectivity minima and are expected to occur since our samples exhibit n-type conduction. For the PbS 8% solid-solution, the phonon contribution is screened by the strong free carrier effects, which is associated with a weak feature in the respective Im(ε) spectrum in the region of ≈155 cm^{-1}. For the two phase-separated samples containing 8%PbS and 30%PbS there are two clear peaks in the Im(ε) spectra located at ≈100 and ≈150 cm^{-1}, while for the PbS 30% solid solution there is a strong peak at ≈150 cm^{-1} and a weaker structure in the frequency range ≈120–130 cm^{-1} (Figure 7b).

The experimentally obtained reflectivity spectra were fitted considering phonons and plasmon contributions to the complex dielectric function:

$$\varepsilon(\omega) = \varepsilon_\infty \prod_j \frac{\omega_{\mathrm{LO,j}}^2 - \omega^2 - i\gamma_{\mathrm{LO,j}}\omega}{\omega_{\mathrm{TO,j}}^2 - \omega^2 - i\gamma_{\mathrm{TO,j}}\omega} + \frac{\varepsilon_\infty \cdot (\omega_P^2 - i(\gamma_P - \gamma_o)\omega)}{-\omega^2 - i\gamma_o\omega} \quad (3)$$

where ε_∞ is the optical-frequency dielectric constant. The first term of Equation (3) corresponds to the phonon contribution with $\omega_{TO,j}$ and $\omega_{LO,j}$ being the TO and LO phonon frequencies and $\gamma_{TO,j}$ and $\gamma_{LO,j}$ the phonon damping constants respectively.

The second term in Equation (3) is the free-carrier term which yields the plasmon contribution with frequency ω_P and a frequency dependent damping constant $\gamma(\omega)$, usually referred to as double damped Drude model or extended Drude model.[43] Using this model, we calculated the reflectivity spectra and Kramers-Kronig obtained Im(ε) shown as solid lines in Figure 7a,b, which are in excellent agreement with the experimental data.

In general, the longitudinal optical (LO) vibrational frequencies are the roots of the complex dielectric function $\varepsilon(\omega)$. In the case of composite materials, i.e., materials having more than one phases, the dielectric function depends on the constituents' volume fraction.[44] Dealing with composite materials, the LO modes obtained by Equation (3) are not the pure LO modes of the different components, but their position is a function of the volume fraction. On the other hand, the TO phonon frequencies are independent of the volume fraction.[45] This means that, even if the material is a composite, the TO modes as obtained by Equation (3) are the pure TO phonon modes of the different components in the composite. Since our intention is to attribute the phonon vibrational frequencies to specific compositions in the PbTe–PbS studied materials, our discussion on the IR reflectivity results is limited only to the analyzed TO phonon modes of Equation (3).

Figure 7c displays the contribution of the TO phonon modes of the studied compositions to the imaginary part of the complex dielectric function. For the analysis of all the studied compositions a TO mode at ≈32 cm^{-1}, though outside our experimental range, was used. The $PbTe_{1-x}$ S_x system shows a "two-mode" behavior on the basis of the Random Element Isodisplacement (REI) model which treats the optical phonons of mixed crystals.[42,46] For PbTe the infrared frequencies are ω_{TO} = 32 cm^{-1} and ω_{LO} = 104 cm^{-1} while for the PbS the respective frequencies are located at 66 and 216 cm^{-1}. Miljkovič et al. studied the optical properties of $PbTe_{1-x}$ S_x mixed crystals for x = 0.02 and x = 0.05 and by linear interpolation of their experimental frequencies determined a simplistic optical mode behavior of $PbTe_{1-x}$ S_x mixed crystals with $0 \le x \le 1$ and their results are displayed as solid lines in Figure 7d.[42] The optical behavior of the system actually coincides with the class A mode behavior of mixed crystals as determined by the notation of Genzel et al.[47]

Our experimental results of the solid-solution materials, the PbTe–PbS 8% solid solution exhibits two TO modes at ≈32 and ≈155 cm^{-1} (see Figure 7c) which confirms that this sample is a solid solution showing normal "two-mode" behavior. For PbTe–PbS 30%, we would expect two observed modes from the simple REI model: one at ≈32 cm^{-1} (which is outside our experimental region) and another ≈130 cm^{-1}. However, modes are observed at ≈150 and ≈120 cm^{-1} (Figure 7c). These two TO modes may be attributed to different phases present in the sample, each of which having also a low frequency TO mode at ≈32 cm^{-1}, suggesting the presence of two phases within the solid-solution PbTe–PbS 30% sample, in agreement with NMR findings. For the two phase-separated PbTe–PbS 8% and 30% samples, the analyzed TO phonon modes of Figure 7c were found at nearly the same frequency confirming the NMR results for the existence of two phases with approximately the same composition in these phase-separated materials.

The analyzed TO phonon frequencies of the solid solution PbTe–PbS materials together with the NMR–obtained alloy compositions are presented in Figure 7d. As can be seen, there is a fairly good agreement between our experimental NMR results and the interpolation lines of Miljkovič et al.[42] For the PbTe–PbS 8% solid solution, the ≈32–155 cm^{-1} TO modes are attributed to a nearly ideal $PbTe_{0.92}S_{0.08}$ crystal. For the PbS 30% solid solution, we find the existence of an additional TO phonon mode of ≈32–124 cm^{-1} in addition to the ≈32–151 cm^{-1} mode, which correspond to NMR–obtained compositions of $PbTe_{0.6}S_{0.4}$ and $PbTe_{0.8}S_{0.2}$, respectively, Figure 7d. For the two phase-separated samples PbS 8% and 30%, the NMR results yielded $PbTe_{0.93}S_{0.07}$ and $PbTe_{0.02}S_{0.98}$ for the compositions of the two phases which have their TO frequencies at ≈32–159 cm^{-1} and ≈32–100 cm^{-1}, respectively. The IR reflectivity results closely agree with the NMR results and confirm that an ideal solid solution is obtained only for the quenched PbTe–PbS 8% sample, while two-phase behavior is observed for the quenched PbTe–PbS 30% sample.

3. Conclusions

For $PbTe_{1-x}$ S_x with x = 0.08 and 0.3, thermally induced precipitation of large regions of PbS in a matrix of PbTe is initiated between 175 and 200 °C, adhering to previous reports of the nucleation of PbS in PbTe.[23] Magic-angle-spinning ^{125}Te NMR spectra of PbTe–PbS exhibit a series of peaks that enable determination of the composition of quenched and annealed samples with higher accuracy (±1% at low x) than available from the phase diagram, both for the Te-rich and Te-poor phases. On the other hand, minor amounts (<2%) of inclusions that can be important for transport properties may escape NMR detection. Incomplete phase separation by nucleation and growth, due to insufficient annealing time, has been detected by NMR for x = 0.16. An unexpected difference between the effects of linear and of angled Te-Pb-S configurations on ^{125}Te NMR chemical shifts was substantiated by DFT simulations. NMR analysis complemented previous investigations by X-ray scattering and electron-beam methods, which showed PbS segregation by annealing, but could not easily quantify the amount of the segregated components.

We have shown that PbTe–PbS thermoelectric materials may reversibly generate solid-solution alloys and phase-separated materials depending on the temperature of annealing. However, nearly ideal solid solutions for PbTe–PbS can be obtained by quenching only within the nucleation and growth composition space (i.e., < ≈12% PbS). It is essential to note that the as-quenched samples of PbTe–PbS 30% appear as alloys by synchrotron PXRD from their agreement with Vegard's law, but the local probe nature of NMR and IR spectroscopy reveals that they are actually phase inhomogeneous. This is an indication of nascent spinodal decomposition that will result in nanostructures, as has been observed previously in samples of the same composition.[34] There are a number of so-called solid solution PbTe-based thermoelectric materials that have recently been reported with adherence to Vegard's law from PXRD but also exhibit low lattice thermal conductivities.[48–50] Our findings highlight the importance of careful

chemical and microstructural analysis of thermoelectric materials; simple powder X-ray diffraction analysis is not sufficient at describing whether a material is truly a solid solution or nanostructured.

4. Experimental Section

Synthesis: Samples of PbTe–PbS 4, 8, 16, 30, and 50% were synthesized using PbTe and PbS starting materials prepared using high-purity starting elements (Pb 99.99% American Elements, Te 99.999% and S 99.99% 5N Plus) by first reacting stoichiometric amounts to create PbTe and PbS starting materials. These starting materials were reground and reacted in the concentrations mentioned. All reactions were flame sealed in fused silica ampoules at a residual vacuum of $\approx 10^{-4}$ Torr and heated to 1100 °C in a box furnace. Samples were inverted several times in the liquid state and quenched in water to room temperature. Selected samples were then post-annealed for 72 h at 500 °C to assure adequate phase separation for comparison with the rapidly quenched samples.

Scanning Electron Microscopy (SEM): Scanning electron microscopy was performed on finely-polished samples using a FEI Helios Nanolab focused ion beam (FIB)/SEM. Imaging using the electron beam was accomplished at 5 kV voltage with a 98 pA current, while milling using the ion beam was accomplished at 30 kV voltage with 2.8 nA current. Areas of the sample were bombarded with Ga^+ ions, resulting in preferential etching of the sample along grain boundaries and differing phases. The resulting image provides a clearer representation of the microstructure, with minimized appearance of surface defects and scratches.

High-Resolution Powder X-Ray Diffraction (PXRD): The samples were hand ground using a mortar and pestle and passed through a 60 µm steel mesh sieve. The resulting fine powders with grain size ≤60 µm were packed into 0.3 mm quartz capillaries and evacuated to a residual vacuum of $\approx 10^{-4}$ Torr and flame-sealed using a high temperature torch. The capillaries were placed in a double-tilt goniometer in transmission geometry (Debye–Scherrer method) and rotated at 500 rpm. High-resolution X-ray diffraction was performed by synchrotron radiation at Argonne National Laboratory on the Advanced Photon Source (APS), beamline 11-BM using a 12-analyzer Si detector and calibrated radiation wavelength of 0.412455 Å.[51,52] A calibrated hot air blower (operational temperature room temperature to 1000 °C accurate to ±5°) was situated approximately 5 mm below the spinning capillary. The small capillary diameter assured an even thermal profile and minimization of X-ray absorption. Rietveld refinements were performed using the GSAS program.

Infrared Reflectivity (IR): Infrared (IR) reflectivity measurements were performed on finely-polished PbTe–PbS samples using a Bruker 113 V FTIR spectrometer with a resolution of about 2 cm^{-1}, at nearly normal incidence, in the 90–1000 cm^{-1} spectral region, at room temperature. The reflection coefficient was determined by a typical sample-in-sample-out method with a mirror as the reference. In nearly normal incidence, the reflectivity is related to the complex dielectric function $\varepsilon(\omega)$ by the relation:

$$R(\omega) = \left(\frac{\sqrt{\varepsilon(\omega)} - 1}{\sqrt{\varepsilon(\omega)} + 1} \right)^2 \quad (4)$$

The experimental reflectivity spectra $R(\omega)$ were analyzed by the Kramers-Kronig (KK) transformation technique to obtain the phase angle between reflected and incident wave. The calculated spectrum of phase angle $\theta(\omega)$ was used with that of $R(\omega)$ to subsequently compute the real and imaginary parts of the complex dielectric function $\varepsilon(\omega)$. The peaks of the resulting $\mathrm{Im}(\varepsilon)$ spectra are associated with the frequencies of the transverse (TO) modes.

Nuclear Magnetic Resonance (NMR): ^{125}Te nuclear magnetic resonance (NMR) experiments were performed at 126 MHz using a Bruker Biospin (Billerica, MA) DSX-400 spectrometer (magnetic field of 9.39 T). The coarsely powdered samples were packed into 2.5-mm zirconia rotors and rotated at 22 kHz in a magic-angle-spinning probe head (Bruker), which narrowed the lines significantly. The $\pi/2$ pulse length was 2.5 µs. Signals were detected after a Hahn echo generated by a $\pi/2$–t_r–π–t_r two-pulse sequence, where t_r denotes a rotation period. Measuring times generally ranged between 15 and 24 h per spectrum, except for spectra to detect Te dispersed in PbTe, which required 2.5 days. In order to minimize distortion of relative peak intensities by the pulse excitation bandwidth, spectra with peaks separated by more than 90 kHz were measured as composites, with carrier frequencies separated by 50 kHz. ^{125}Te NMR chemical shifts were referenced to $Te(OH)_6$ in solution, using solid TeO_2 at +750 ppm as a secondary reference. The longitudinal (T_1) relaxation times of the observed peaks were similar, between 1.5 and 2.5 s; the peak near the PbTe resonance position had a slightly longer T_1 than the other signals in both annealed and low-x quenched samples. The spectra shown were recorded with recycle delays of 3 or 10 s. ^{207}Pb NMR spectra were also measured but did not exhibit resolved peaks that provided interesting information.

Density Functional Theory (DFT) Calculations of Chemical Shifts: All geometry optimizations and NMR chemical shift calculations were performed using plane wave density functional theory (DFT) employing a Perdew–Burke–Ernzehof (PBE) functional and pseudopotentials generated on-the-fly, using CASTEP and CASTEP NMR programs (Accelrys Software Inc.).[53] An energy cutoff of 550 eV was used along with the exact representation of the electron density. We studied two sizes of PbTe unit cells with a single Te atom substituted by a S atom. The smaller, 64-atom unit cell of $PbTe_{0.97}S_{0.03}$ adopts $Pm\bar{3}m$ symmetry and was done on a Mokhorst-Pack grid of $7 \times 7 \times 7$ *k*-points. The larger, 128-atom unit cell of $PbTe_{0.98}S_{0.02}$ was studied in P4/mmm symmetry and on a Mokhorst-Pack grid of $8 \times 8 \times 4$ *k*-points. Geometry optimizations were conducted with the following criteria: convergence of 5×10^{-6} eV/atom energy, maximum force of 0.01 eV/Å, maximum stress of 0.02 GPa, and maximum displacement of 5×10^{-4} Å. The results were visualized using Materials Studio (Accelrys Software Inc.).[53]

Supporting Information

Supporting Information is available from the Wiley Online Library or from the author.

Acknowledgements

S.N.G. and M.G.K. thank the Revolutionary Materials for Solid State Energy Conversion, an Energy Frontier Research Center funded by the U.S. Department of Energy, Office of Science, Office of Basic Energy Sciences under Award Number DE-SC0001054, for primary funding. The SEM work was performed in the EPIC facility of the NUANCE Center at Northwestern University. The NUANCE Center is supported by NSF-NSEC, NSF-MRSEC, Keck Foundation, the State of Illinois, and Northwestern University. Use of the Advanced Photon Source at Argonne National Laboratory was supported by the U. S. Department of Energy, Office of Science, Office of Basic Energy Sciences, under Contract No. DE-AC02-06CH11357. NMR characterization by K.S.R., B.N., E.M.L., and A.R. was supported by the U.S. Department of Energy, Office of Basic Energy Science, Division of Materials Sciences and Engineering, at the Ames Laboratory, which is operated for the U.S. Department of Energy by Iowa State University under Contract No. DE-AC02-07CH11358.

Received: July 12, 2012
Published online: September 20, 2012

[1] M. G. Kanatzidis, *Chem. Mater.* **2009**, *22*, 648.
[2] G. J. Snyder, E. S. Toberer, *Nat. Mater.* **2008**, *7*, 105.
[3] C. J. Vineis, A. Shakouri, A. Majumdar, M. G. Kanatzidis, *Adv. Mater.* **2010**, *22*, 3970.
[4] J. R. Sootsman, D. Y. Chung, M. G. Kanatzidis, *Angew. Chem. Int. Ed.* **2009**, *48*, 8616.
[5] J. R. Szczech, J. M. Higgins, S. Jin, *J. Mater. Chem.* **2011**, *21*, 4037.

[6] S.-M. Lee, D. G. Cahill, R. Venkatasubramanian, *Appl. Phys. Lett.* **1997**, *70*, 2957.
[7] R. Venkatasubramanian, E. Siivola, T. Colpitts, B. O'Quinn, *Nature* **2001**, *413*, 597.
[8] A. I. Hochbaum, R. Chen, R. D. Delgado, W. Liang, E. C. Garnett, M. Najarian, A. Majumdar, P. Yang, *Nature* **2008**, *451*, 163.
[9] D. Li, Y. Wu, R. Fan, P. Yang, A. Majumdar, *Appl. Phys. Lett.* **2003**, *83*, 3186.
[10] K. F. Hsu, S. Loo, F. Guo, W. Chen, J. S. Dyck, C. Uher, T. Hogan, E. K. Polychroniadis, M. C. Kanatzidis, *Science* **2004**, *303*, 818.
[11] T. Ikeda, V. A. Ravi, G. J. Snyder, *Acta Mater.* **2009**, *57*, 666.
[12] J. D. Sugar, D. L. Medlin, *J. Alloys Compd.* **2009**, *478*, 75.
[13] Y. Pei, J. Lensch-Falk, E. S. Toberer, D. L. Medlin, G. J. Snyder, *Adv. Funct. Mater.* **2011**, *21*, 241.
[14] Y. Gelbstein, O. Ben-Yehuda, E. Pinhas, T. Edrei, Y. Sadia, Z. Dashevsky, M. Dariel, *J. Electron. Mater.* **2009**, *38*, 1478.
[15] S. Gorsse, P. Bauer Pereira, R. Decourt, E. Sellier, *Chem. Mater.* **2009**, *22*, 988.
[16] J. Androulakis, C.-H. Lin, H.-J. Kong, C. Uher, C.-I. Wu, T. Hogan, B. A. Cook, T. Caillat, K. M. Paraskevopoulos, M. G. Kanatzidis, *J. Am. Chem. Soc.* **2007**, *129*, 9780.
[17] J. R. Sootsman, J. He, V. P. Dravid, C.-P. Li, C. Uher, M. G. Kanatzidis, *J. Appl. Phys.* **2009**, *105*, 083718.
[18] J. R. Sootsman, J. He, V. P. Dravid, S. Ballikaya, D. Vermeulen, C. Uher, M. G. Kanatzidis, *Chem. Mater.* **2009**, *22*, 869.
[19] T. Ikeda, E. S. Toberer, V. A. Ravi, G. Jeffrey Snyder, S. Aoyagi, E. Nishibori, M. Sakata, *Scripta Mater.* **2009**, *60*, 321.
[20] H. J. Wu, S. W. Chen, T. Ikeda, G. J. Snyder, *Acta Mater.* **2012**, *60*, 1129.
[21] J. R. Sootsman, R. J. Pcionek, H. Kong, C. Uher, M. G. Kanatzidis, *Chem. Mater.* **2006**, *18*, 4993.
[22] J. R. Sootsman, H. Kong, C. Uher, J. J. D'Angelo, C. I. Wu, T. P. Hogan, T. Caillat, M. G. Kanatzidis, *Angew. Chem. Int. Ed.* **2008**, *47*, 8618.
[23] S. N. Girard, J. He, C. Li, S. Moses, G. Wang, C. Uher, V. P. Dravid, M. G. Kanatzidis, *Nano Lett.* **2010**, *10*, 2825.
[24] S. N. Girard, J. He, X. Zhou, D. Shoemaker, C. M. Jaworski, C. Uher, V. P. Dravid, J. P. Heremans, M. G. Kanatzidis, *J. Am. Chem. Soc.* **2011**, *133*, 16588.
[25] M. S. Darrow, W. B. White, R. Roy, *Trans. Metall. Soc. AIME* **1966**, *236*, 654.
[26] M. S. Darrow, W. B. White, R. Roy, *Mater. Sci. Eng.* **1969**, *3*, 289.
[27] A. Volykhov, L. Yashina, V. Shtanov, *Inorg. Mater.* **2006**, *42*, 596.
[28] A. Volykhov, L. Yashina, M. Tamm, A. Ryzhenkov, *Inorg. Mater.* **2009**, *45*, 968.
[29] V. Leute, N. Volkmer, *Z. Phys. Chem* **1985**, *144*, 145.
[30] J. D. Gunton, M. Droz, *Introduction to the Theory of Metastable and Unstable States*, Vol. *183*, Springer-Verlag, Berlin **1983**.
[31] T. Ikeda, L. A. Collins, V. A. Ravi, F. S. Gascoin, S. M. Haile, G. J. Snyder, *Chem. Mater.* **2007**, *19*, 763.
[32] T. Ikeda, N. J. Marolf, K. Bergum, M. B. Toussaint, N. A. Heinz, V. A. Ravi, G. Jeffrey Snyder, *Acta Mater.* **2011**, *59*, 2679.
[33] E. Quarez, K. F. Hsu, R. Pcionek, N. Frangis, E. K. Polychroniadis, M. G. Kanatzidis, *J. Am. Chem. Soc.* **2005**, *127*, 9177.
[34] J. He, S. N. Girard, M. G. Kanatzidis, V. P. Dravid, *Adv. Funct. Mater.* **2010**, *20*, 764.
[35] E. M. Levin, B. A. Cook, K. Ahn, M. G. Kanatzidis, K. Schmidt-Rohr, *Phys. Rev. B* **2009**, *80*, 115211.
[36] C. M. Jaworski, J. Tobola, E. M. Levin, K. Schmidt-Rohr, J. P. Heremans, *Phys. Rev. B* **2009**, *80*, 125208.
[37] M. N. Alexander, P. L. Sagalyn, S. D. Senturia, C. R. Hewes, *J. Nonmet.* **1973**, *1*, 251.
[38] M. D. Nielsen, E. M. Levin, C. M. Jaworski, K. Schmidt-Rohr, J. P. Heremans, *Phys. Rev. B* **2012**, *85*, 045210.
[39] K. Beshah, D. Zamir, P. Becla, P. A. Wolff, R. G. Griffin, *Phys. Rev. B* **1987** , *36* , 6420.
[40] H. Lin, E. S. Bozcaronin, S. J. L. Billinge, J. Androulakis, C. D. Malliakas, C. H. Lin, M. G. Kanatzidis, *Phys. Rev. B* **2009**, *80*, 045204.
[41] S. D. Senturia, A. C. Smith, C. R. Hewes, J. A. Hofmann, P. L. Sagalyn, *Phys. Rev. B* **1970**, *1*, 4045.
[42] J. M. Miljković, N. Romčević, Z. V. Popovic, W. Köunig, V. N. Nikiforov, *Phys. Status Solidi B* **1996**, *193*, 43.
[43] F. Gervais, *Mater. Sci. Eng., R* **2002**, *39*, 29.
[44] G. A. Niklasson, C. G. Granqvist, O. Hunderi, *Appl. Opt.* **1981**, *20*, 26.
[45] S. A. FitzGerald, T. W. Noh, A. J. Sievers, L. A. Xue, Y. Tzou, *Phys. Rev. B* **1990**, *42*, 5469.
[46] N. Romčević, J. Trajić, M. Romčević, A. Golubović, S. Nikolić, V. N. Nikiforov, *J. Alloys Compd.* **2005**, *387*, 24.
[47] L. Genzel, T. P. Martin, C. H. Perry, *Phys. Status Solidi B* **1974**, *62*, 83.
[48] Y. Pei, X. Shi, A. LaLonde, H. Wang, L. Chen, G. J. Snyder, *Nature* **2011**, *473*, 66.
[49] H. Wang, Y. Pei, A. D. LaLonde, G. J. Snyder, *Adv. Mater.* **2011**, *23*, 1366.
[50] Y. Pei, A. LaLonde, S. Iwanaga, G. J. Snyder, *Energy Environ. Sci.* **2011**.
[51] P. L. Lee, D. Shu, M. Ramanathan, C. Preissner, J. Wang, M. A. Beno, R. B. Von Dreele, L. Ribaud, C. Kurtz, S. M. Antao, X. Jiao, B. H. Toby, *J. Synchrotron Radiat.* **2008**, *15*, 427.
[52] J. Wang, B. H. Toby, P. L. Lee, L. Ribaud, S. M. Antao, C. Kurtz, M. Ramanathan, R. B. V. Dreele, M. A. Beno, *Rev. Sci. Instrum.* **2008**, *79*, 085105.
[53] S. J. Clark, M. D. Segall, C. J. Pickard, P. J. Hasnip, M. I. J. Probert, K. Refson, M. C. Payne, *Z. Kristallogr.* **2005**, *220*, 567.